

Hypersonic Fluid-Structure Interaction on a Cantilevered Plate

Gaetano MD Currao*, Andrew J Neely*,

David R Buttsworth**, Sudhir L Gai*

*University of New South Wales

Canberra, ACT, 2602, Australia

**University of Southern Queensland

Toowoomba, QLD, 4350, Australia

Abstract

This work is a numerical and experimental study of fluid-structure interaction at Mach 5.8. Numerical results from low- and high-fidelity models are shown and compared. Procedures and details of the generation of the numerical mesh are given. The mesh topology shape, irrespective of flow direction, shock position, and sonic line location can lead to non-physical results if not optimised. Orthogonality of the cells to the wall is fundamentally important to reach numerical convergence and reliable results. Under an inviscid point of view, piston theory is confirmed to be an appropriate tool in the evaluation of the inviscid pressure over the plate, as it showed good agreement with the empirical data. Concerning the viscous aspects, the shear stress and heat transfer histories shared the same frequency with the structural, and their spatial distribution present a degree for hysteresis. Finally, the boundary layer height changes not only according to local slope and speed of the wall, but it is a function of the actual structural mode of vibration.

Nomenclature

Flow Variables:

| | | |
|--------|---|-----------------------------|
| q | = | Heat flux rate on the plate |
| p | = | Pressure |
| τ | = | Shear stress on the plate |
| a | = | Sound speed |
| St | = | Stanton number |
| C_f | = | Skin friction coefficient |
| M | = | Mach number |

Structural Variables

| | | |
|-----------------|---|-----------------------------------|
| l | = | Beam element's length |
| L | = | Plate length |
| T | = | Period of oscillation |
| th | = | Plate's thickness |
| w | = | Structural displacement |
| θ | = | Local slope |
| ω | = | Frequency ($= 2\pi f$) |
| E | = | Young's modulus |
| I | = | Inertia of the beam cross-section |
| M | = | Mass matrix |
| K | = | Stiffness matrix |
| \bar{D} | = | Damping matrix |
| ζ | = | Damping ratio |
| α, β | = | Rayleigh coefficients |

Other Variables

| | | |
|--------|---|--|
| x | = | Coordinate tangent to the wall |
| y | = | Coordinate normal to the wall |
| t | = | Time |
| η | = | Ratio between pressure with 3D effects and 2D pressure |

Subscripts:

| | | |
|----------|---|---|
| w | = | At the wall |
| S | = | Structure |
| 1 | = | 1 st mode |
| 2 | = | Post-shock conditions or 2 nd mode |
| 3 | = | 3 rd mode |
| ∞ | = | Freestream conditions |

Abbreviations:

| | | |
|------|---|--|
| BL | = | Boundary layer |
| LE | = | Leading edge |
| PT1 | = | Pressure transducer near the hinge line |
| PT2 | = | Pressure transducer near the trailing edge |
| PT3 | = | Pressure transducer beneath the plate |
| TE | = | Trailing edge |
| TUSQ | = | Wind tunnel at University of Southern Queensland |

1. Introduction

Empirical data on fluid-structure interaction (FSI) in hypersonic flow is limited. The majority of the experimental work took place in the late 50s and 70s with hypersonic flutter being the main concern for the early supersonic and hypersonic experiences that culminated in the development of the test aircraft such as the X-15. The main models made use of semi-rigid wings and fins where the airplane's support was represented by a system of springs and flexures [1-11]. By the 1980's, however, the majority of the flutter facilities were dismantled resulting in a dramatic fall in high-speed FSI research and development [12,13].

Whilst the majority of these experiments were focussed on structural instabilities, very little research was done in terms of viscous effects and how the dynamics of the boundary layer was coupled with the structural displacement [10,11].

The last ten years have seen a renewed interest in fluid-thermal-structure interaction in hypersonic flows because of the increasing computational power now available. Special emphasis has been given to numerical simulations and low-fidelity models (LFMs) [14]. The inviscid aspects are generally modelled by the piston theory [15], while the viscous heating is modelled using the Eckert reference enthalpy method [16,17]. The structural dynamics are often reduced to the first 6 modes which are the most energetic [18]. As regards the actual shape of the boundary layer, the momentum displacement thickness is computed a priori and superimposed on the model, changing the shape of the surface [12,19].

However, experiments conducted in this area remain limited [20-24] and possible validation of numerical codes, on the basis of empirical data produced thus far, has proven challenging. This justifies the need for fundamental hypersonic FSI experiments to further understand the underlying physics and to enhance the fidelity of numerical simulation.

Recent studies have analysed the influence of structural dynamics on the boundary layer shape and stability. From a numerical point of view, Riley *et al.* [25-26] highlighted the incidence of high-frequency acoustic disturbance on the transition location for a generic metal panel subjected to buckling. More recently, Currao *et al.* [21] analysed the boundary layer thickness over an oscillating cantilevered plate using high-speed imagery from a schlieren system. These empirical observations showed that the boundary layer height is not simply a function of freestream conditions, local slope, and speed of the wall. Thus, the wall fluxes (shear stress and heat flux) are also dependent on the structural mode of deformation.

The present work is a numerical and experimental study, which develops on the empirical findings of Currao *et al.* [21] in a more systematic way. Numerical results are compared against a LFM and validated through experiments in terms of displacement and pressure. Wall fluxes and boundary layer are analysed spatially and temporally. Finally, it is shown that the boundary layer thickness cannot be considered only a function of the local plate slope and free-stream condition, as perturbations in the downstream flow can affect the boundary layer upstream and vice versa. When quasi-steady conditions apply, the boundary layer can more realistically be considered a function of the instantaneous structural deformed shape.

2. Experimental Set-Up

The Facility

The facility used for the experiments was the free-piston driven compression-heated Ludwieg tube, TUSQ [27], located at the University of Southern Queensland in Toowoomba, Australia. TUSQ is capable of producing approximately 200 ms of hypersonic flow at a nominal Mach number of 5.85. The tunnel offers a high level of reproducibility and consistency across different runs, with the mean pressure change less than 5%. The fluctuations in the freestream pressure are confined to around 100 Pa (Figure 1); whilst the free stream Mach number is set to 5.8 with a small spatial uncertainty of ~0.3%. In order to preserve a high level of fidelity keeping the general applicability of the results shown, numerical data will refer to nominal free stream conditions except when directly compared with particular experimental runs (Table 1).

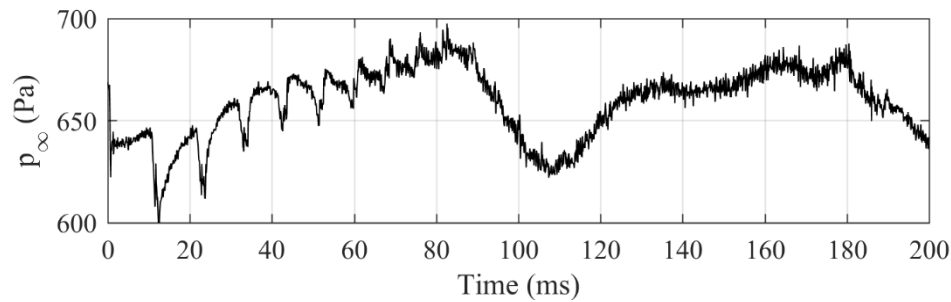


Figure 1. Freestream pressure history.

Table 1. Condition used for the numerical simulations. RUN475 refers to the mean freestream conditions during the actual experiment.

| Condition | M_∞ | p_∞ (Pa) | T_∞ (K) | T_w (K) | Re_∞ (1/m) |
|-----------|------------|---------------------|----------------------|--------------|----------------------|
| Nominal | 5.85 | 755 | 75 | 290 | 7.16e6 |
| RUN475 | 5.85 | 659.30 (± 50) | 70.24 (± 1.55) | 289.15 | 7.16e6 |

Experimental model: HyFoil

The model, designated HyFoil0.3, was manufactured entirely out of aluminium and was composed of two parts, the support (rigid) and the oscillating plate (Figure 2). The support was a 100 mm long and 10 mm thick plate, with a leading edge wedge angle of 45 degrees, an AOA of 20 degrees and a leading edge radius of 500 μm . Its function was compressing the flow over the oscillating plate, which was cantilevered at the support's trailing edge (TE), in order to ensure oscillations of the desired amplitude. The plate, 130 mm long and 2mm thick, had material properties that deviated slightly from the nominal values for Al-6061-T6. The oscillating plate was cut from a large panel with a nominal thickness of 2 mm, and it underwent a series of non-destructive tests to establish flexural modulus (E) and damping ratio (ζ). The first was obtained via a static test. The plate was cantilevered and a point load was applied at the trailing edge by hanging a known mass from the plate. Thus, the displacement was compared with the numerical solution for a plate with the same properties. In a similar fashion, the damping ratio was obtained by removing the point load and studying the free oscillations. These measurements were made using a laser scanner with an accuracy of the order of 50 μm . The material properties are reported in Table 2.

Table 2. Plate's properties

| Length (mm) | Width (mm) | Thickness (mm) | E (GPa) | ρ (g/cc) | ζ |
|-------------------|------------------|---------------------|--------------------|------------------|---------|
| 130 (± 0.1) | 80 (± 0.1) | 1.95 (± 0.02) | 52.7 (± 0.5) | 2668.75 | 0.0038 |

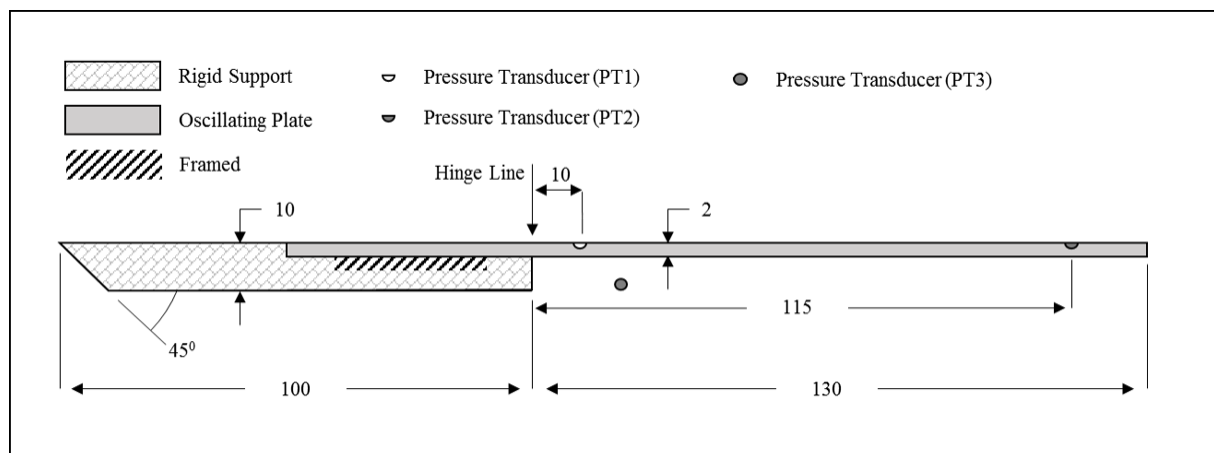


Figure 2. Technical details of the experimental set-up.

The type of constraint and the nature of the flow, forced the plate to oscillate mainly following the first mode, which is shown in Figure 3. As the plate motion was primarily two-dimensional (2D), the numerical simulations shown in this work assumed a 2D flow around the plate neglecting border effects. Such an assumption drastically reduced the computational time without introducing decisive approximations, which are discussed in the section devoted to the numerical validation.

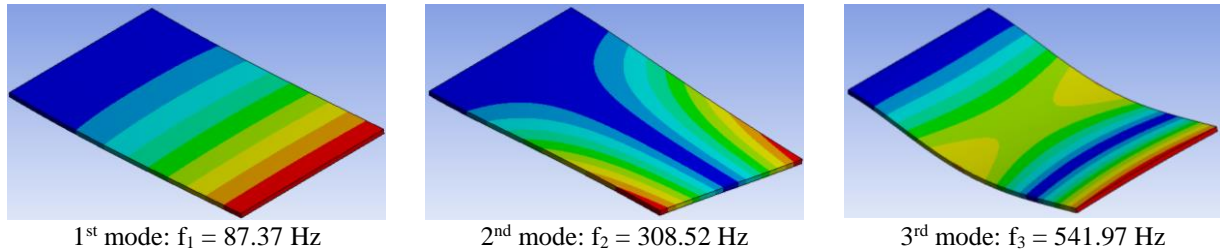


Figure 3. Modes of the plate and respective frequency (contours show displacement).

Pressure Measurement and Flow Visualization

Experimental data were comprised of point pressure measurements and image tracking of the displacement. The former were obtained by three pressure transducers, two located on the top of the plate and the third in the recirculation region beneath the plate (Figure 2 and Figure 4). The uncertainty in the measurement is limited to ± 50 Pa.

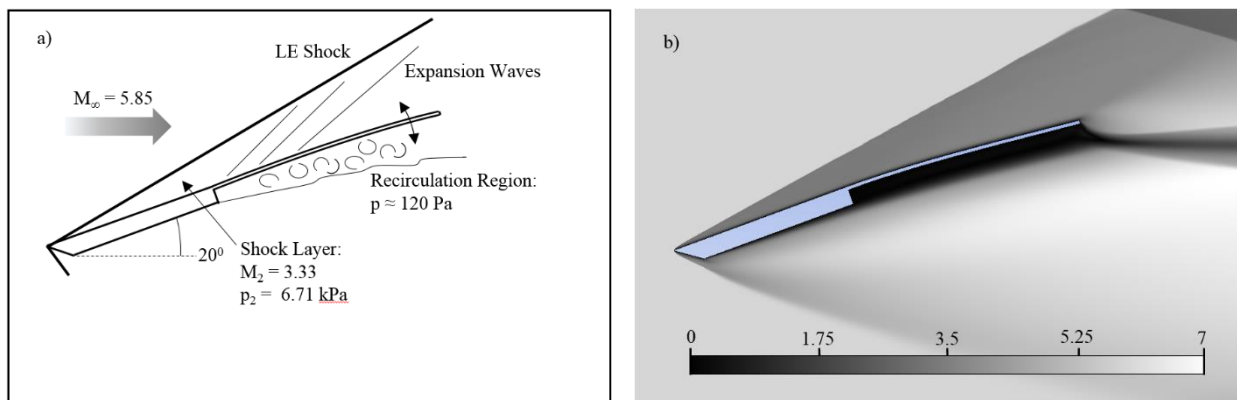


Figure 4. a) Schematic of the experiment and b) Mach distribution from numerical results.

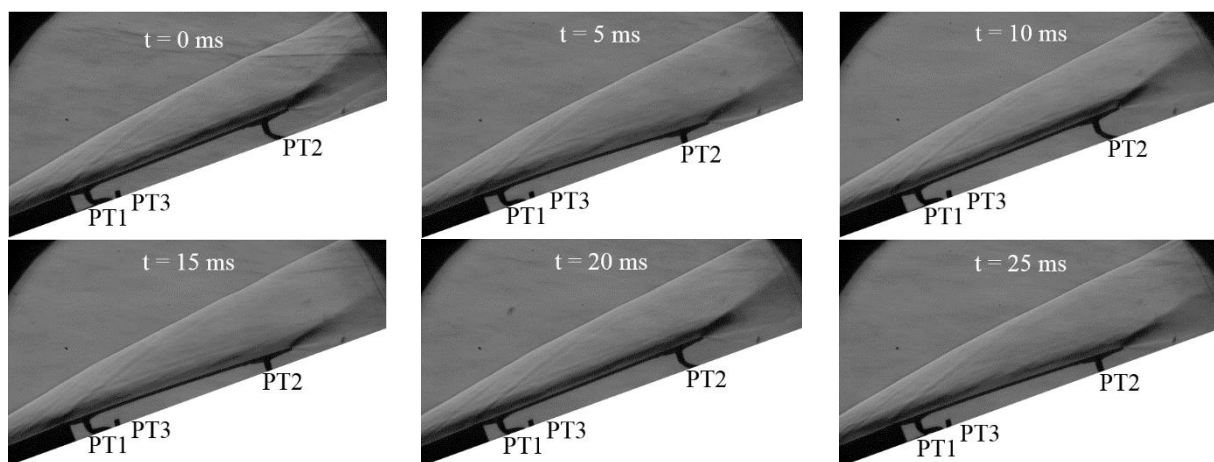


Figure 5. Schlieren flow visualization and plate's deflection tracking. The plastic hoses are connected to the pressure transducers: PT1 (near the hinge), PT2 (near the trailing edge) and PT3 (beneath the plate).

Additionally, the experiment was recorded through a schlieren system to investigate the flow structure and to evaluate the plate's deformation history (see Figure 5).

3. Low-Fidelity Model (Inviscid)

The plate is modelled as a cantilevered beam. With a thickness to length ratio of $O(1e-3)$, sections are assumed always normal to the beam axis making use of the widely-known Euler-Bernoulli beam model appropriate [28]. The equation describing the motion of the beam can be written as:

$$D \frac{\partial^4 w}{\partial x^4} = p(x, t) - \mu \frac{\partial^2 w}{\partial t^2}, \quad (1)$$

where, $D = EI/(1-\nu^2)$, and μ is the mass per unit length and p is the aerodynamic pressure, which requires additional modelling. The equation is solved using the Galerkin orthogonal decomposition method. Each element can be described using four nodal displacement variables:

$$w(x, t) = N_j(x)w_j(t), \quad j = 1, 2.. \quad (2)$$

where $\mathbf{N}(x)$ is the shape function vector, $\mathbf{w}(x) = [w_1 \ \theta_1 \ w_2 \ \theta_2]^T$ is the nodal vector and j the node number. For a single element beam, the finite element model (FEM) can be written as:

$$M\ddot{\mathbf{w}} + \bar{D}\dot{\mathbf{w}} + K\mathbf{w} = f \quad (3)$$

with

$$M = \frac{\rho AL}{420} \begin{bmatrix} 156 & 22l & 54 & -13l \\ 22l & 4l^2 & 13l & -3l^2 \\ 54 & 13l & 156 & -22l \\ -13l & -3l^2 & -22l & 4l^2 \end{bmatrix}, \quad K = \frac{D}{l^3} \begin{bmatrix} 12 & 6l & -12 & 6l \\ 6l & 4l^2 & -6l & 2l^2 \\ -12 & -6l & 12 & -6l \\ 6l & 2l^2 & -6l & 4l^2 \end{bmatrix}, \quad (4.1 - 4.2)$$

$$f = \frac{l}{2} p(x, t) \begin{bmatrix} 1 \\ l/6 \\ 1 \\ -l/6 \end{bmatrix}, \quad \bar{D} = \alpha M + \beta K. \quad (4.3 - 4.4)$$

Where f is the aerodynamic load and D the damping matrix. M (mass matrix) and K (stiffness matrix), here represented in their original form, are modified with the Timoshenko shear stress correction [28]. Being the main contribution, in terms of effective mass, given by the first two modes, a Rayleigh (2-modes) damping model is used [29]. α and β , or mass and stiffness damping coefficients respectively, are obtained given the first two natural frequencies (ω_1, ω_2) and the damping ratios (ζ_1, ζ_2):

$$\alpha = 2\omega_1\omega_2 \frac{\zeta_1\omega_2 - \zeta_2\omega_1}{\omega_2^2 - \omega_1^2}, \quad \beta = 2 \frac{\zeta_2\omega_2 - \zeta_1\omega_1}{\omega_2^2 - \omega_1^2}. \quad (5)$$

The aerodynamic pressure is modelled via the piston theory [15]:

$$p(x, t) = p_2 \left(1 + \frac{\gamma - 1}{2} \frac{v(t)}{a_2} \right)^{2\gamma/\gamma-1}, \quad (6)$$

Where the subscript 2 refers the condition behind the leading edge shock. The piston speed $v(t)$ is defined as:

$$v(t) = [1 \ 0 \ 1 \ 0] \frac{\dot{\mathbf{w}}}{2} + [0 \ 1 \ 0 \ 1] U_2 \frac{\mathbf{w}}{2}. \quad (7)$$

Finally, a non-linear model is adopted to take moderately large deflections into account [30]. When the beam is deflecting the actual distance between the two nodes j and $j+1$ of the beam element, Δx_j , is smaller than l :

$$\Delta x_j = l(1 - \cos \theta_j) \sim l \theta_j^2 / 2, \quad (8)$$

This results in an over estimation of the nodal moments. Thus, the aerodynamic load vector f is corrected, reducing the nodal moments appropriately as follows:

$$f_j = \begin{bmatrix} f_j \\ t_j \\ f_{j+1} \\ t_{j+1} \end{bmatrix} \Rightarrow \begin{bmatrix} f_j \\ t_j - f_j l \theta_j \\ f_{j+1} \\ t_{j+1} - f_{j+1} l \theta_{j+1} \end{bmatrix}, \quad \text{with } \theta_j = \sum_1^{j-1} \frac{\theta_i^2}{2}. \quad (9)$$

4. High Fidelity Modelling: Numerical Methodology

Mesh Details

The mesh is created via ANSYS/ICEM CFD. Using the strategy of “blocking”, the mesh was divided in outer flow and boundary layer. The latter is an o-grid (or circular) block around the plate, characterised by first cell height (Δy_w), top cell eight (Δy_e), height of the boundary layer block (δ_{O-GRID}) and average length of the cell (Δx) (Table 3).

Table 3. Details of the o-grid parameters.

| Location | δ_{O-GRID} (μm) | Δy_w (μm) | Δy_e (μm) | Δx (μm) |
|--------------|--|-----------------------------------|-----------------------------------|---------------------------------|
| Leading Edge | ~ 2 | 0.2-2 | 7-20 | 2-4 |
| Flat plate | ~ 20 | 30 | 30-70 | ~ 250 |

The convergence of the simulation was extremely sensitive to the shape of the o-grid at the stagnation point. It was necessary to match the edge of the o-grid with the curved standing shock. Finally, all the cells on the wall had to be orthogonal to the wall. Details of the mesh are given in Figure 6.

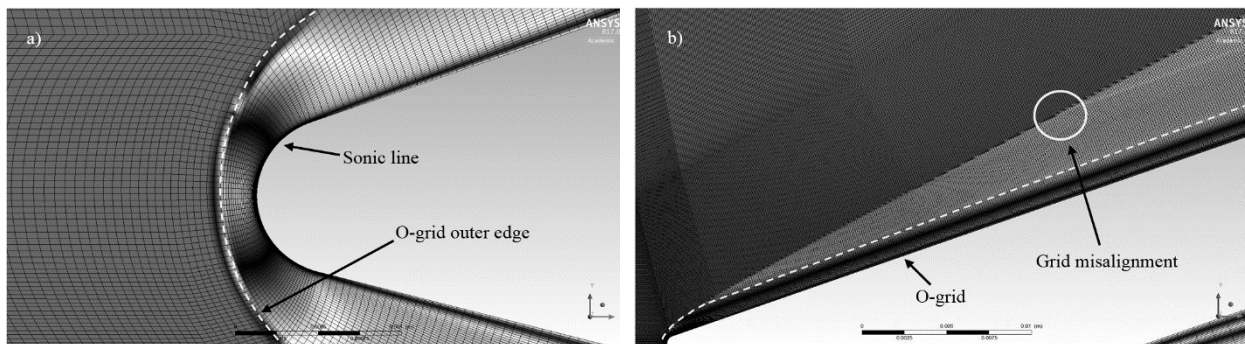


Figure 6. Mesh details. a) Near the LE, the o-grid edge is aligned with the curved shock and the cells follow the shape of the sonic line. b) Where the mesh is not aligned perfectly with the shock non-physical waves are created.

It was extremely challenging if not generally impossible, to align perfectly a strong (curved) shock with the mesh grid [31]. When this happened, the shock generated spurious waves every time it moved from one cell to another one, or went through a “cell-step”. Local refinement with hanging nodes, based on local gradient, proved to have limitations. Additionally, a general refinement enhanced this phenomenon. The strategy used in this work was to minimize the strength of the spurious waves, reducing cell growth ratio and cell misalignment in the region spanning the shock. To facilitate this trial-and-error process it is advisable to create a grid block to include the shock layer. Two typical cases of fair and poor alignment are shown in Figure 7.

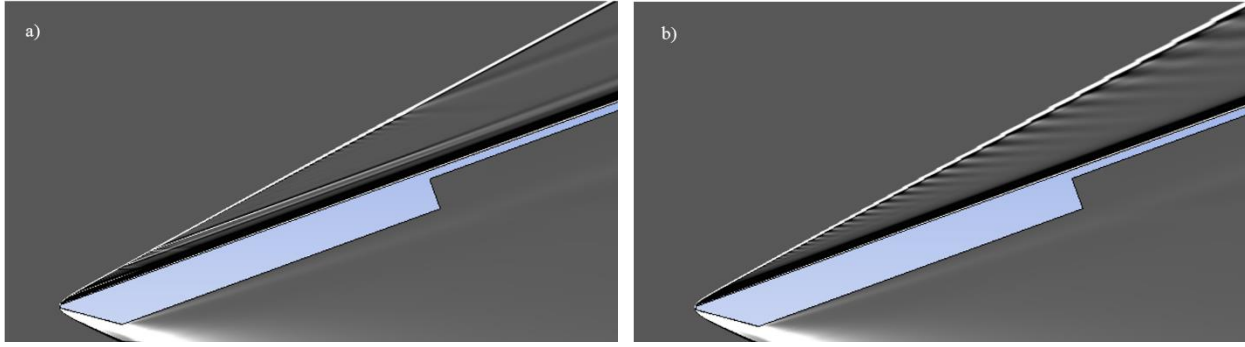


Figure 7. Numerical shadowgraph of the results from two different meshes with a) fair and b) poor shock alignment.

Convergence Criterion

The numerical simulations were performed using ANSYS Fluent 17.0. An implicit second-order upwind solver was used to produce the steady solution. The steady solution was used to initialize the transient FSI simulation; being the flow fully established in the first half a millisecond of flow. The steady initialization dramatically reduced the computational time without visibly affecting the quality of the solution. The residuals of continuity, energy and momentum equations were checked with every iteration to monitor the convergence. In order to make the convergence criteria generally applicable, the residual (Res) of a conserved variable (W), and the square root of the average of the squares of the residuals (RMS) are defined as:

$$Res(W) = \frac{\partial W}{\partial t}, \quad (10)$$

$$RMS(W) = \sqrt{\sum \left(\frac{\partial W}{\partial t}\right)^2}. \quad (11)$$

Every simulation converged to a value of scaled RMS residuals smaller than $1e-6$. The scaled RMS residual is defined as the ratio of the RMS residual to the largest value of the RMS residual during the first five iterations. The domain was solved via a density-based, cell-centred, second-order upwind solver. A blending factor of 80% between first and second order was used to solve the cells near the shock.

Mesh Independency Study

The most sensitive parameter in the mesh independence study was the first cell height to the wall (Table 4).

Table 4. Grid independence study in the y-direction: refinement in the first cell height of the o-grid. Convergence criterion = $|\Delta q| = 1\%$.

| Mesh name | Δx (μm) | Δy_w (μm) | q at $x = 212$ mm (kw/m^2) | $max(RMS)$ |
|-----------|---------------------------|-----------------------------|-------------------------------------|------------|
| MESH1 | 500 | 60 | 7.93(+6.15%) | < $1e-6$ |
| MESH2 | 500 | 30 | 7.47 | < $1e-6$ |
| MESH3 | 500 | 15 | 7.51(+0.53%) | < $1e-6$ |

Table 5. Grid independence study in the x-direction: refinement in the cell-length of the o-grid over the flat plate. Convergence criterion = $|\Delta q| = 1\%$.

| Mesh name | Δx (μm) | Δy_w (μm) | q at $x = 212$ mm (kw/m^2) | $max(RMS)$ |
|-----------|---------------------------|-----------------------------|-------------------------------------|------------|
| MESH3 | 1000 | 30 | 7.55(+1.10%) | < $1e-6$ |
| MESH2 | 500 | 30 | 7.47 | < $1e-6$ |
| MESH4 | 250 | 30 | 7.48(+0.2%) | < $1e-6$ |

As regards the x-direction, the mesh was over-refined as the optimal value was chosen to minimise the spurious oscillations generated by LE shock and mesh misalignment. The grid independence study is shown in Table 5.

5. Comparison with experiments

In Figure 8(a), the pressure trend near the hinge (PT1 at $x = 215$ mm) and near the trailing edge (PT2 at $x = 110$ mm) are in good agreement with the experiment. Close to the hinge, the fluctuations of pressure are mainly due to the unsteadiness of the freestream pressure. PT1 and numerical results are in good agreement. As regards PT2, the discrepancies are smaller than 13% while PT3 and numerical simulations present negligible differences (Figure 8(b)).

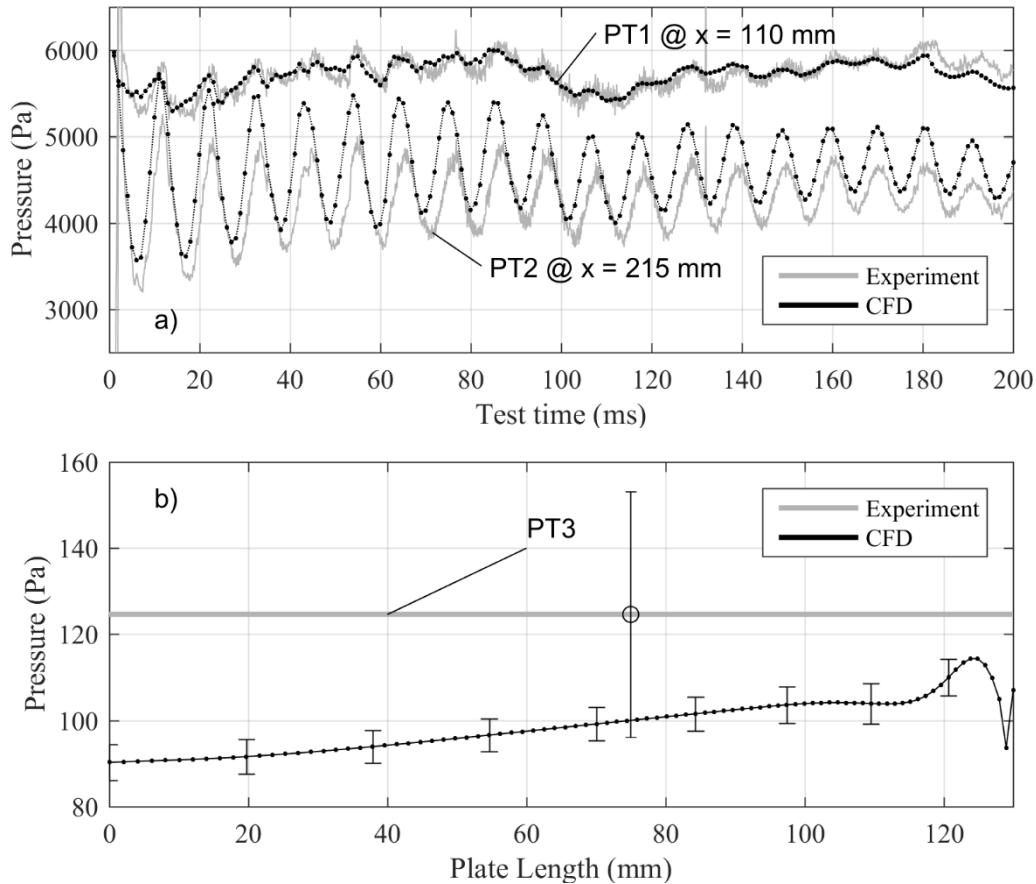


Figure 8. Comparison between numerical results and experiments in terms of pressure: a) at two different locations, near the hinge and close to the TE, and b) under the plate.

The discrepancies between PT2 and numerical simulations can be explained in terms of 3D effects. Bonney [32,33] developed a relation for subsonic and supersonic flow to determine the extent of the 3D effects caused by corners and sharp changes in leading-edge curvature. According to Bonney, the pressure tip losses on the plate are confined to a Mach cone with an angle of $\mu = \sin^{-1} 1/M_2$ and with the apex on the corner of the plate (as shown in Figure 9).

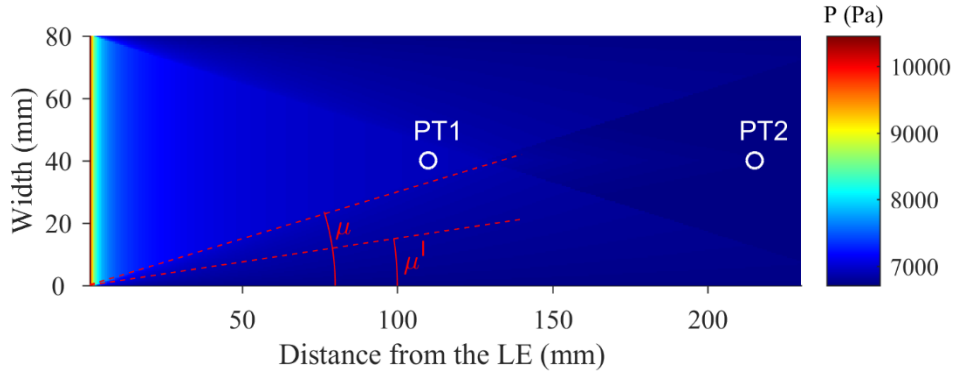


Figure 9. Pressure distribution on a sharp plate with $AOA = 20^\circ$ using the conical theory.

Referring to Figure 9, a relationship between the actual pressure affected by the tip loss (p_{3D}) and the pressure without border effects (p) can be written as:

$$\frac{p - p_{edge}}{p_{3D} - p_{edge}} = \frac{2}{\pi} \sin^{-1} \sqrt{\frac{\tan \mu'}{\tan \mu}} \quad (12)$$

Where $\mu' < \mu$, is the angle of a ray emanating from the plate corner within the Mach cone. p_{edge} is assumed to be the pressure behind the shock, which is clearly an approximation, especially because downstream of the hinge the thickness of the oscillating plate is only one fifth that of the upstream rigid plate, resulting in more spillage over the edges. PT2 is within a region of overlap, where the pressure is determined as

$$p_{3D}^I(\mu') = 2p_{3D}(\mu') - p. \quad (13)$$

Thus, it is possible to define a parameter η as:

$$\eta_{TH} = \frac{p_{3D}^I}{p}, \quad \eta_{exp} = \frac{p_{exp}}{p_{CFD}}, \quad \text{at } x = 215 \text{ mm} \quad (14)$$

where subscripts *TH* and *exp* denote the theoretical and actual value of η respectively. η is a parameter indicative of the incidence of the 3D effects on the evaluation of the pressure; it is equal to one if there are not 3D effects or PT2 is outside the Mach cone, otherwise it will be generally $\eta < 1$ being $p_{edge} < p_2$. Table 6 shows a comparison in terms of η between conical theory and experiment showing a fair agreement. In order to match η_{EXP} , p_{edge} must be 400 Pa smaller than what was assumed in the Equation (12). To conclude, considering the uncertainties in the pressure measurement (± 50 Pa), the discrepancies in terms of pressure, between PT2 and numerical results, can be considered justified.

Table 6. Conical theory results at $x = 215$ mm.

| | η | Equivalent P_{edge} (Pa) |
|--------------|--------|----------------------------|
| From theory | 0.98 | 6712 (= P_2) |
| Actual Value | ~0.93 | 6312 (-6.0%) |

Finally, in Figure 10 the computed TE displacement history is in good agreement with the experimental data, especially in terms of frequency. Discrepancies in amplitude are limited to 0.2 mm (or 40% of the plate thickness) and related to the aforementioned pressure differences between numerical results and experimental data.

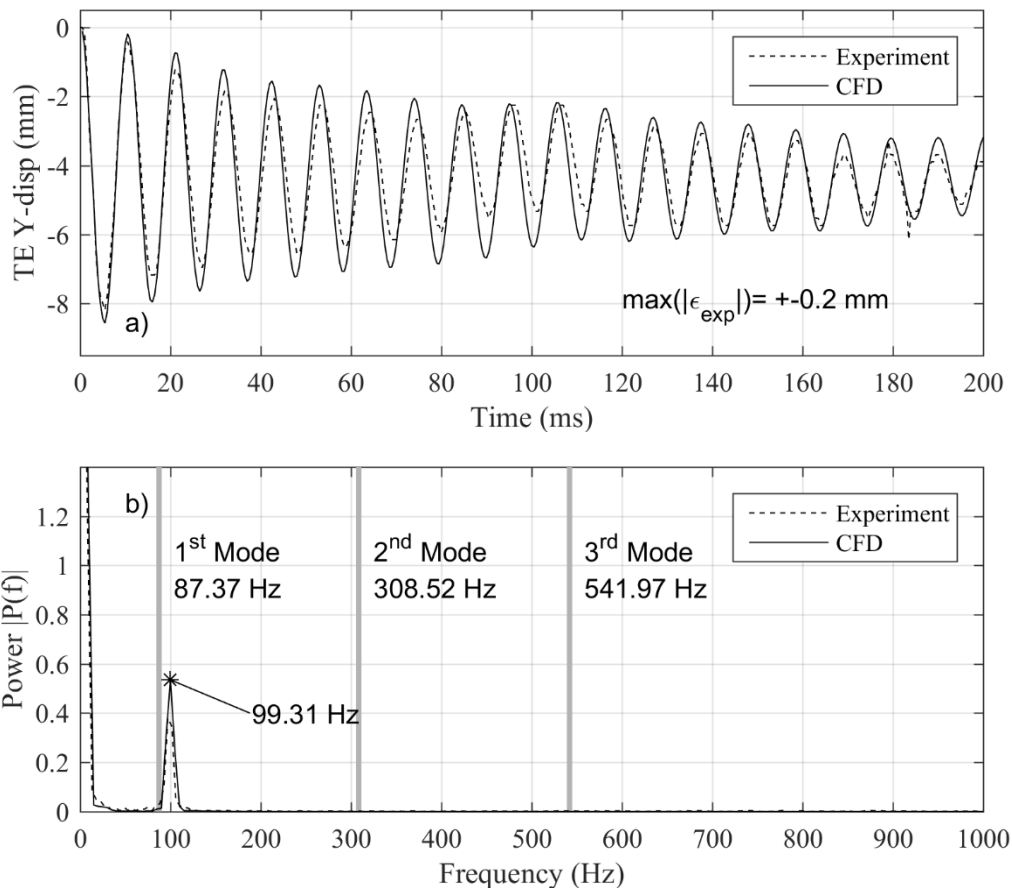


Figure 10. Comparison with experiment in terms of (lower) TE displacement. a) TE displacement history b) Amplitude spectrum of the TE displacement.

6. Comparison between High- and Low-Fidelity Models

The LFM is a design tool, only used to rapidly estimate amplitude and frequency of the plate's oscillation (Table 7), whilst maintaining a reasonable level of fidelity in terms of pressure and structural deformations (Figure 11).

Table 7. Comparison between ROM and High fidelity simulation in terms of computational performance.

| <i>Type of model</i> | <i>Software</i> | <i>Analysis</i> | <i>N^o of cores</i> | <i>Flow time</i> | <i>Comp. time</i> |
|----------------------|-----------------|-----------------|-------------------------------|------------------|-------------------|
| Low-fidelity | Matlab | Inviscid | 1 | 200 ms | 5 mins |
| High-Fidelity | ANSYS/Fluent | Viscous | 25 | 200 ms | 8 to 50 days |

In Figure 11, numerical simulations are in good agreement with the (inviscid) low-fidelity model. The pressure is found to be only a function of the local slope, being in Equation (7)

$$\dot{w} \ll U_2 \theta. \quad (15)$$

To conclude, viscous effects can be assumed somewhat negligible to the correct evaluation of deformation history and the problem can be considered quasi-steady.

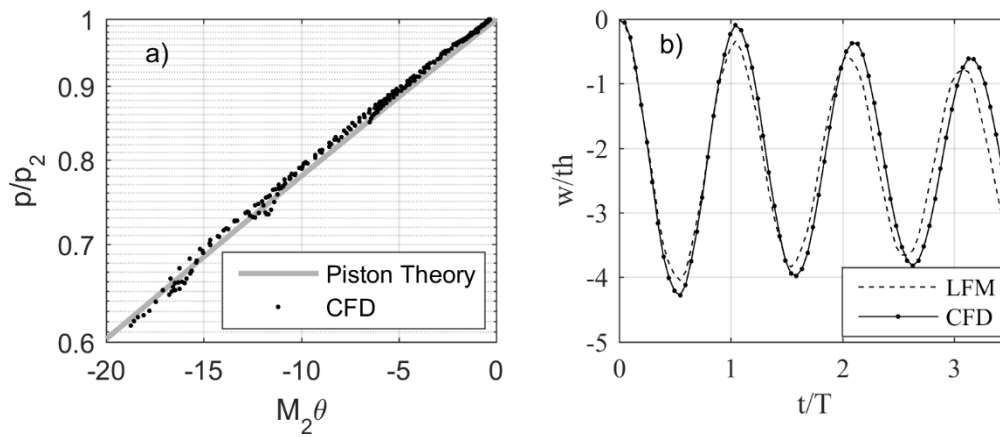


Figure 11. Comparison between analytical and numerical model: a) Pressure along the plate for every time step and the piston theory law. b) TE displacement from LFM and high fidelity simulation.

7. Viscous Aspects

To begin with, there is no phase delay between the moving wall and the boundary layer (BL), confirming the aforementioned quasi-steady nature of the problem. This is shown in Figure 12, where heat flux rate and skin friction not only are in phase with each other (respecting the Reynolds analogy) but they share the same frequency with the oscillating plate (ω_s).

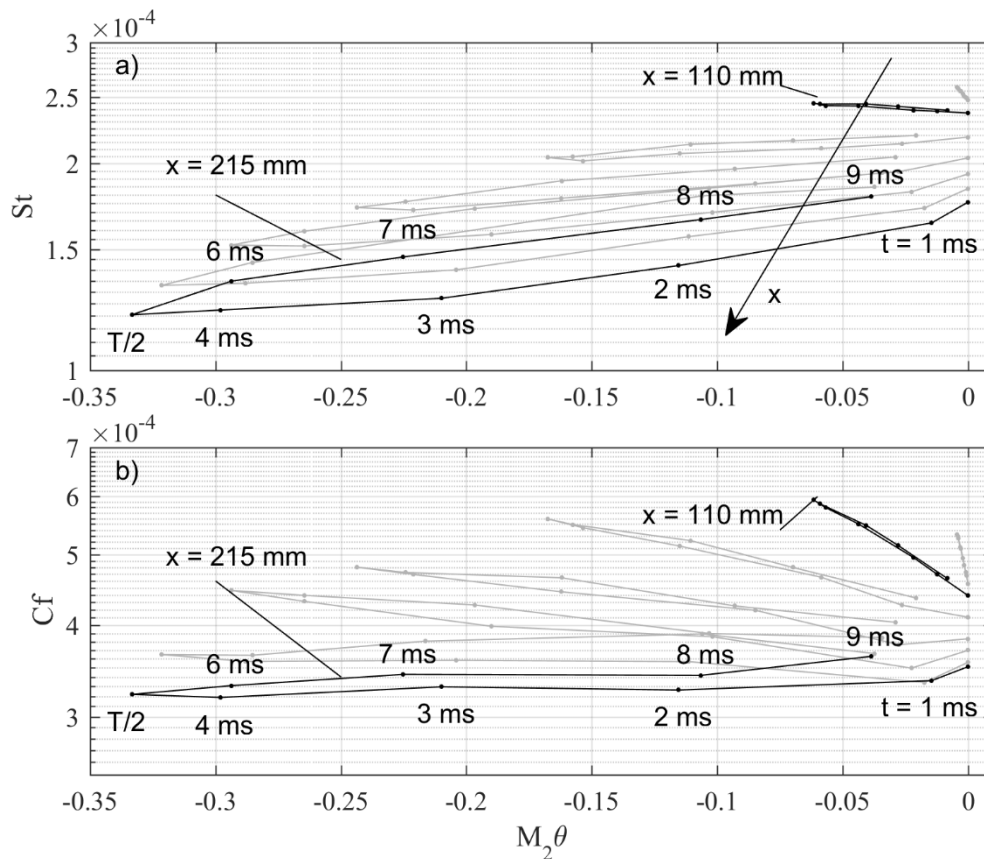


Figure 12. a) Stanton number and b) skin friction coefficient histories on the plate. Each line is representative of a specific location on the plate relative to the hinge ($x = 100$ mm). The location of the PTs (110 and 215 mm) are indicated in black.

As expected, the wall fluxes near the trailing edge present a certain amount of hysteresis, which is absent or small in the proximity of the hinge ($M_2\theta \approx 0$) where the piston theory is more linear. This is most probably due to the inertia of the boundary layer, which is normally thicker in hypersonic flows. However, the change in the BL thickness does not have an effect on the external pressure as the cantilevered plate is in a region of weak-interactions [17] or:

$$\bar{\chi} = \frac{M_2}{\sqrt{Re_2}} \sqrt{C_2} < 0.01 < 3. \quad (16)$$

In Figure 12 the wall fluxes present a special feature as, for $\theta < 0$, they increase near the hinge ($M_2\theta = 0$) and decrease near the TL, even though $M_2\theta \leq 0$ everywhere at every time step. Thus, the BL thickness does not only depend on the freestream pressure, as perturbations within the BL can travel upstream reducing the local δ even where the external pressure is decreasing due to the local deflection of the plate. This feature of the BL is confirmed by the numerical results shown in Figure 13.

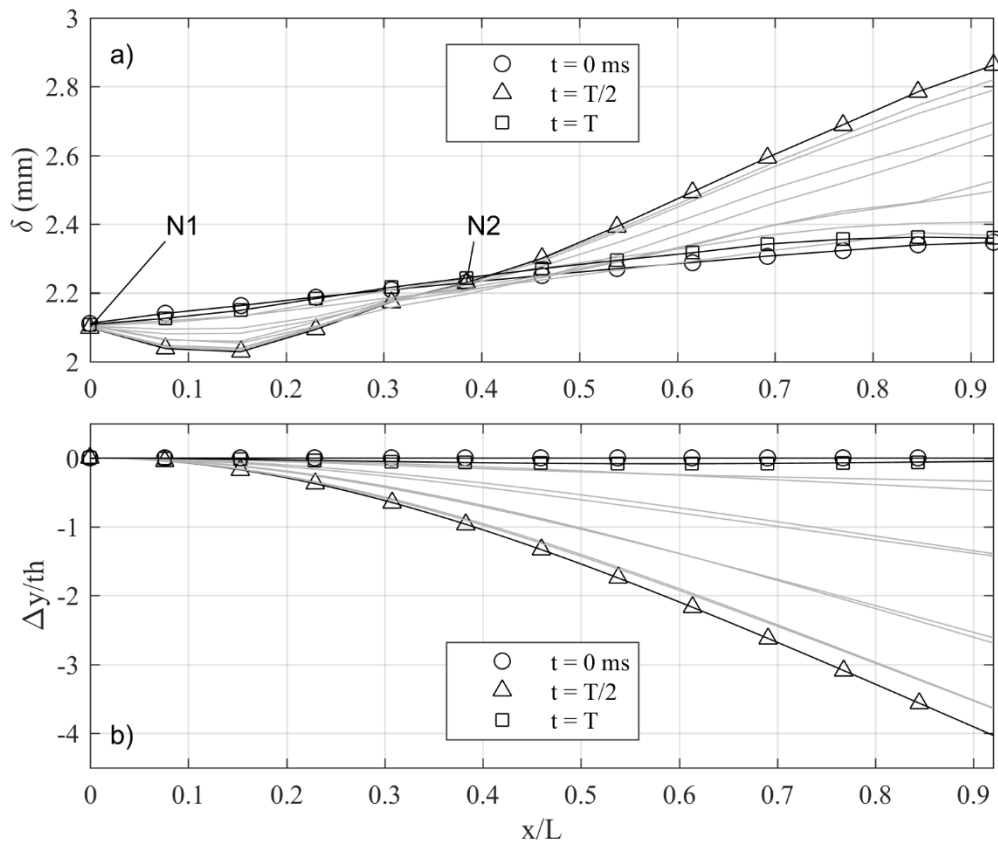


Figure 13. Numerically derived shapes of a) the BL and of b) the cantilevered plate for every millisecond of the first period (T). Trends in black refers to $t = 0, T/2$ and T , whilst the trends in grey refers to the time steps in the middle. N1 and N2 represent the nodes where the BL height remains constant with time.

Table 8. Comparison among different sources in terms of second node position (N2).

| Source | Constraint | L (mm) | δ/L | x_{N2}/L | M_2 |
|-------------|------------|----------|-------------|------------|-------|
| Currao [21] | Fixed-Free | 70 | 0.014-0.050 | 0.88 | 3.33 |
| This work | Fixed-Free | 130 | 0.015-0.022 | 0.38 | 3.33 |

The BL and the plate share the same characteristic frequency (ω_s) but they have different modes of oscillation. The boundary layer's mode presents two nodes, N1 (at the root) and N2 (at $x/L = 0.38$). These findings are in agreement with empirical data from Currao *et al.* [21] as shown in Table 8.

For this case, under the hypothesis of quasi-steady flow and weak interactions, the local BL height at $x = x_j$, is only a function of the plate shape and of the boundary layer height upstream the plate, or

$$\delta(x_j, t) = \delta(x_j; \theta(x, t), \delta(0),)$$

$$\text{with } \begin{cases} \dot{w} \ll U_2 \theta \\ \bar{\chi} < 3 \end{cases} \quad (17.1 - 2)$$

8. Conclusion

Validation data was provided for a simple configuration, an oscillating plate cantilevered at the trailing edge of a support inclined of 20° with respect to the hypersonic flow. The piston theory is confirmed to be a reliable tool to compute the inviscid external pressure under the assumption of weak viscous interactions. The problem is quasi-steady, as the dynamic term in the definition of the piston speed is small. Wall fluxes near the trailing edge of the plate present a certain degree of hysteresis, most probably due to the inertial effects of the boundary layer. The boundary layer thickness cannot be considered solely a local function of slope and structural speed as disturbances within the BL can travel upstream and downstream. Under the assumption of a quasi-steady regime, calculating the boundary layer's initial shape a-priori and using the piston theory to estimate the boundary layer thickness evolution could lead to strong approximations especially when the determination of viscous aspects, like the separation point in shock-wave boundary layer interaction problems, plays a role.

References

- [1] Runyan, H.L. and H.G. Morgan. 1957. Flutter at very high speed. *NACA RM L57D16a*: 10-12.
- [2] Lauten, W.T., M.L. Gilbert and W.O. Armstrong. 1958. A Mach number of 6.86 for possible flutter. *NACA RM L58B27*: 1-20.
- [3] Gibson, F.W. and J.S. Mixson. 1959. Flutter investigation at a Mach number of 7.2 of models of the horizontal and vertical surfaces of the X-15 airplane. *NASA MEMO 4-14-59L*: 1-24.
- [4] Morgan, H.G. and R.W. Miller. 1959. Flutter tests of some simple models at a Mach number of 7.2 in Helium flow. *NASA MEMO 5-8-59L*: 1-25.
- [5] Arman, A. 1961. Study of flow over oscillating airfoil models at a Mach number of 7.0 in Helium. *NASA TN D-992*: 1-22.
- [6] Hanson, P.W. 1961. Aerodynamic effects of some configuration variables on the aeroelastic characteristics of lifting surfaces at Mach numbers from 0.7 to 6.86. *NASA TN D-984*: 1-52.
- [7] Goetz, R.C. 1969. Hypersonic flutter analysis using measured static aerodynamic derivatives, and comparison with experiment. *NASA TN D-5233*: 1-51.
- [8] Yates Jr., E. C. and R.M. Bennett. 1972. Analysis of supersonic-hypersonic flutter of lifting surfaces at angle of attack. *J. Aircraft*, vol. 9 No.7: 481-489.
- [9] Ericsson, L.E., B.O. Almroth and J.A. Bailie. 1978. Hypersonic aerothermoelastic characteristics of a finned missile. *AIAA 16th Aerospace Sciences Meeting 78-231*: 1-8.
- [10] Ericsson, L.E. 1975. Hypersonic aeroelastic analysis. *ADA 028794*: 3.24-3.37.
- [11] Orlik-Rückemann, K.J. 1970. Dynamic viscous pressure interaction in hypersonic flow. *Aeronautical report LR-535, National Research Council of Canada*: 1-75.
- [12] Spain, C., D. Soistmann, E. Parker and M. Gibbson. An overview of selected NASP aeroelastic studies at the NASA Langley research center. *AIAA 2nd International Aerospace Planes Conference*: 1-14.
- [13] Spain, C.V., T.A. Zeiler and E.P. Bullock. 1993. A flutter investigation of all-movable NASP-like wings at hypersonic speeds. *34th AIAA/ASME/ASCE/AHS/ASC*: 1-9.
- [14] McNamara, J.J. and P.P. Friedmann. 2011. Aeroelastic and aerothermoelastic analysis in hypersonic flow: past, present, and future. *AIAA Journal* vol.49, No.6: 1089-1122.
- [15] Ashley, H. and G. Zartarian. 1956. Piston theory – a new aerodynamic tool for the aeroelastician. *Journal of the Aeronautical Sciences*: 1109-1118.
- [16] Eckert, E.R.G. 1956. Engineering relations for heat transfer and friction in high velocity laminar and turbulent boundary layer flow over surfaces with constant pressure and temperature. *Transactions of the American Society of Mechanical Engineering*, vol.78, no.6: 1273.
- [17] Anderson, J.D. 2006. Hypersonic and high-temperature gas dynamic 2nd ed., *AIAA*: 345-346, 380-395.
- [18] Dowell, E.H. 1966. Nonlinear oscillations of a fluttering plate. *AIAA Journal* vol.4, No. 7: 1267-1275.
- [19] McNamara, J.J. and P.P. Friedmann. 2007. Aeroelastic and aerothermoelastic analysis of hypersonic vehicles: current status and future trends. *48th AIAA/ASME/ASCE/AHS/ASC*: 11-12.

- [20] Willems, S., A. Gülham and B. Esser. 2013. Shock induced fluid-structure interaction on a flexible wall in supersonic turbulent flow. *Progress in Flight Physics 5*: 285-308.
- [21] Currao, G.M.D., A.J. Neely, D. Buttsworth, and R. Choudhury. 2016. Measurement and Simulation of Hypersonic Fluid-Structural Interaction on a Cantilevered Plate in Mach 6 Flow. *AIAA SciTech Forum 2016:1088*: 1-16
- [22] Casper, K.M., S.J. Beresh, J.F. Henfling, W. Spillers and P. Hunter. 2016. Fluid-Structure Interactions on a Slender Cone under Quiet Flow Conditions at Mach 6. *AIAA SciTech Forum 2017-0402*: 1-19.
- [23] Hammerl, G., A. Seitz, F. Verdugo, W.A. Wall, D. Daub, S. Willems and A. Gülhan. 2016. FSI of rocket nozzles – on the influence of simplified modelling of structural boundary conditions for an FSI experiment & scalable solvers for strongly coupled problems. *Sonderforschungsbereich/Transregio 40 – Annual Report 2016*: 253-262
- [24] Ji, C., W. Jiang, J. Zhu, L. Ziqiang and F. Li. 2017. Experimental study of hypersonic flutter of a blunt-leading-edge trapezoidal wing. *21st AIAA International Space Planes and Hypersonic Technologies Conference*: 1-9.
- [25] Riley, Z.B., J.J. McNamara and H.B. Johnson. 2014. Assessing hypersonic boundary-layer stability in the presence of structural deformation. *AIAA Journal vol.52 no.11*: 2548-2556.
- [26] Riley, Z.B. and J.J. McNamara. 2016. Interaction between aerothermally compliant structures and boundary layer transition in hypersonic flow. *AIAA SciTech Forum 2016-1087*: 3-9.
- [27] Buttsworth, D.R. 2009. Ludwig tunnel facility with free piston compression heating for supersonic and hypersonic testing. *9th Australian Space Science Conference*: 153-162.
- [28] Przemieniecki, J.S. 1968. Theory of matrix structural analysis. *McGraw-Hill Book Co.*:11-24,79,296.
- [29] Liu, M. and D.G. Gorman. 1995. Formulation of Rayleigh damping and its extension. *Computers & Structures vol.57 no.2*: 277-278.
- [30] Bisshopp, K.E. 1973. Approximations for large deflection of a cantilever beam. *Quarterly of applied mathematics*: 521-526.
- [31] Candler, V.G., P.K. Subbareddy and J.M. Brock. 2015. Advances in computational fluid dynamics methods for hypersonic flows. *Journal of Spacecraft and Rockets vol.52 no.1*: 17-23
- [32] Bonney, E.A. 1946. Aerodynamic characteristics of rectangular wings at supersonic speeds. *Journal of the Aeronautical Sciences*: 110-112.
- [33] Bertin, J.J. and R.M. Cummings. 2009. Aerodynamics for engineers 5th ed. *Pearson Education*: 516-520.